Combustion and Flame 244 (2022) 112274

Contents lists available at ScienceDirect

Combustion and Flame

journal homepage: www.elsevier.com/locate/combustflame

Heat release rate response of azimuthal thermoacoustic instabilities in a pressurized annular combustor with methane/hydrogen flames

Byeonguk Ahn*, Thomas Indlekofer, James R. Dawson, Nicholas A. Worth

Department of Energy and Process Engineering, Norwegian University of Science and Technology, Trondheim 7491, Norway

ARTICLE INFO

Article history:
Received 10 August 2021
Revised 20 June 2022
Accepted 20 June 2022

Keywords:
Annular combustion chamber
Combustion instabilities
Hydrogen
Harmonics
Flame dynamics
Pressurized combustor

ABSTRACT

In this study, the heat release rate (HRR) response during self-excited azimuthal thermoacoustic instabilities in a pressurized annular combustor is investigated for hydrogen/methane blended flames. The equivalence ratio and hydrogen power fraction were varied for a constant air mass flow rate, resulting in self-excited azimuthal instabilities of varying amplitudes. Although significant harmonic components were observed in the pressure response, the spatially integrated HRR response was dominated by the fundamental component of the mode. Despite the wide range of operating conditions, an approximately linear relationship was observed between limit cycle velocity and HRR oscillation amplitudes for both the fundamental and first harmonic components, and the phase varied slowly as a function of amplitude. As the phase lag between the HRR and pressure oscillations reduced, the instability amplitude increased due to the increased driving through the Rayleigh criterion. Fuel blends with higher hydrogen fractions produced larger phase differences and lower amplitude responses. High-speed flame imaging was used to analyze the spatial distribution of the HRR oscillations which exhibited significant harmonic content and only provided small contributions to the integrated HRR. The high frequencies associated with these harmonics resulted in the presence of multiple structures with opposing phases simultaneously on the flame brush. This explains why the integrated contributions to the HRR were small. Fourier mode decomposition was employed to better understand the observed reduction in instability amplitude with increasing hydrogen power fraction. When the hydrogen content is higher, multiple fluctuations of the HRR are present simultaneously on the flame, resulting in global cancellation. In contrast, for lower hydrogen content, higher amplitude instabilities are generated, resulting in different flame dynamics. At high amplitudes, the response is more asymmetric as a result of the azimuthal nature of the instability.

1. Introduction

Heavy-duty industrial and aero-derivative gas turbines are important for large scale power generation. In light of increasing environmental concerns and the need to reduce emissions, fuel flexibility utilizing carbon-free fuels such as hydrogen has become a recent research focus [1]. Mixing hydrogen with natural gas has the potential to reduce net CO_2 emissions. However, adding hydrogen changes the fuel characteristics, increasing flame speed and reducing ignition delay time, which can lead to issues with flashback and auto-ignition phenomena [2–5]. In addition, these changes can also alter the operational stability limits of a gas turbine, promoting combustion dynamics in previously stable regimes, or modifying the amplitude levels and frequencies of existing instabilities [4,6–9].

Combustion instabilities are a major development issue for gas turbines and result from a constructive coupling between the unsteady heat release rate (HRR) and the acoustic field. The effect of hydrogen on combustion instabilities has recently gained significant attention, and the current review by Beita *et al.* [10] reports that it can have both stabilizing and destabilizing impacts. From a thermophysical or chemical point of view, it is known that hydrogen has higher adiabatic flame temperatures, flame speed, and diffusivity than methane, which can affect the flame dynamics strongly. For example, Chterev and Boxx [11] have shown that hydrogen addition affects the flame shape and the flame length in the pressurized PRECCINSTA premixed swirl burner. They observed that changes in density modified the wave propagation speeds in the plenum which resulted in an increased phase delay between the pressure and the HRR. This in turn affects the amplitude of the thermoacoustic oscillations. Before hydrogen addition, the amplitude increased if the phase difference was negative, and decreased if it was positive. Similar results were reported

* Corresponding author.
E-mail address: byeonguk.ahn@ntnu.no (B. Ahn).

https://doi.org/10.1016/j.combustflame.2022.112274

by [12,13]. The increased adiabatic flame temperature for hydrogen enriched methane flames also leads to an increase in the oscillation frequency. Lee *et al.* [14] compare the dynamic behavior of a mesoscale burner for pure methane and pure hydrogen flames and observed that it coupled with higher eigenmodes for hydrogen operation. Investigations on Flame Transfer Functions (FTFs) also revealed increased cut-off frequencies observed in hydrogen-enriched methane flames due to increased compactness of the flame [15].

In the particular case of annular chambers, pressure waves can propagate azimuthally as traveling waves of varying amplitude. A number of experimental investigations have been devoted to azimuthal instabilities in industrial [16–18] and lab-scale combustors [19–24]. Numerical modelling has also been undertaken through high fidelity simulations [25,26], and through the application of thermoacoustic network models [27–29]. These investigations have described the modal dynamics which can arise in such systems, where azimuthal waves propagating in different directions around the annulus can continuously vary in amplitude and orientation [20,21,25]. This can make the response more difficult to quantify due to the large variation of modal instability states. Recent studies have shown that modal dynamics are largely influenced by the symmetry of the configuration [28,30–35], and the level of turbulent noise [16,28,36,37]. However, most experimental studies focusing on azimuthal modes have been conducted under atmospheric conditions, which differ somewhat from practically relevant conditions.

Very few investigations have studied azimuthal instabilities under pressurized conditions. This may be important as choked boundary conditions at the combustor exit are more realistic [38]. Fanaca *et al.* [39,40] examined the response of forced premixed flames in a pressurized annular combustor, demonstrating that aerodynamic differences between single isolated flames and flames in the annular combustor result in different delay times. However, no self-excited azimuthal instabilities were reported in this study. Recently, a number of studies have reported self-excited azimuthal modes under pressurized conditions in a lab-scale facility [41,42]. The first of these [41] only exhibited azimuthal modes in a flashback state, which prevented the detailed study of the flame dynamics. Modification of the experiment permitted the excitation of azimuthal modes without flashback, allowing a more detailed investigation of the pressure field dynamics [42]. In comparison with previous studies at atmospheric pressure, the amplitudes of the instabilities generated under pressurized conditions are significantly larger. The generation of very high amplitude pressure oscillations resulted in a clear preference for spinning modes. Additionally, when the amplitudes reached a sufficiently large amplitude, strong harmonic contributions were observed in the pressure field. The amplitude of these components was found to follow a quadratic relationship, as described by Lieuwen and Yang [43]. While Stow *et al.* [44] note that the effect of harmonic contributions to circumferential thermoacoustic modes can be neglected if these are small, such assumptions must be carefully assessed based on their relative magnitude.

Although not in annular combustors, the presence of higher harmonics has been observed in a number of previous investigations. For example, Bonciolini and Noiray [45] performed an experimental investigation into harmonic thermoacoustic modes which occur in a sequential combustor, reporting that the nonlinear relations varied as a function of combustor power. Kim *et al.* [46] explored the nonlinear interaction between the fundamental component and higher harmonics in premixed and partially-premixed swirl stabilized systems at atmospheric pressure. They highlighted the importance of higher harmonics, emphasizing the ability of Flame Describing Functions (FDFs) to predict thermoacoustic instabilities could be limited when the amplitude of higher harmonics approaches that of the fundamental component amplitude. Passarelli *et al.* [47] describe a cross-frequency coupling phenomena in a liquid fueled pressurized gas turbine combustor, where the pressure response was dominated by the fundamental and fourth harmonic, but the HRR was dominated by the first and third harmonic.

Despite the potential significance of nonlinear phenomena, the current standard approach is to assume that higher harmonics are not dynamically important to the thermoacoustic response. Stow and Dowling [44] investigated the effect of including harmonics in a time domain simulation, and while they concluded that the geometry and flame model used meant that the harmonics had little effect, they noted that these may have a greater role in some cases, particularly if the frequency of the harmonic is close to a resonant frequency of the chamber. The effects of significant harmonics were considered in a study by Haeringer *et al.* [48], who consider a laminar premixed slit burner that produced fundamental and harmonic components of a similar order of magnitude. It was found that considering the effect of higher HRR harmonics in an extended FDF model, offered improved performance over a standard single frequency FDF model in the prediction of limit cycle phenomena. This study therefore demonstrates that if harmonic components of a mode are dynamically significant, consideration and modelling of these are required in order to make accurate stability predictions.

The present study focuses on the fundamental and harmonic response of the HRR during self-excited azimuthal instabilities in a pressurized annular combustor with varying hydrogen power fraction. While this configuration is known to contain significant harmonic components in the pressure field [41,42], the present study quantifies for the first time the harmonic response of the HRR in detail, in order to determine the importance of nonlinear dynamics in this configuration. After determining that the harmonics only play a minor role in the global flame response, the study then aims to physically explain why these contributions are small, and to better understand the flame response to azimuthal excitation. This involves characterization of the flame dynamics, in order to identify key parameters responsible for strong acoustic interactions at specific conditions, and to assess the asymmetry of the flame response.

2. Experimental setup

2.1. The Intermediate Pressure Annular combustor

Figure 1 a shows a schematic of the Intermediate Pressure Annular (IPA) combustor [41,42]. The current study uses the same configuration reported previously in [42], but the main features are summarized.

A fully premixed fuel-air mixture enters a cylindrical plenum where glass beads are installed to remove large scale flow structures, and improve flow uniformity. The flow passes through a 22 mm thick sintered metal plate with mean pore size 183 μm, porosity 0.12, and $\Delta p \approx 15$ kPa at the flow rate selected in this study. The sintered plate is highly acoustically reflective, and is characterized in detail in [42].

The reactants are divided into 12 injector tubes which have an inner diameter of $d_{\text{inj}} = 19$ mm. Each injector tube has a central rod ($d_{\text{r}} = 5$ mm), which expands to a diameter of $d_{\text{bb}} = 14$ mm at the bluff body, as shown in fig. 1c. The expansion has a cone angle of 38° over a streamwise distance of 10 mm. This bluff body geometry is modified as described by [42], and differs from an initial design which was more susceptible to flashback [41]. Six vane counter-clockwise axial swirlers are mounted $L_g = 33$ mm upstream of the sudden expansion into the combustor, which is referred to herein as the *dump plane*.

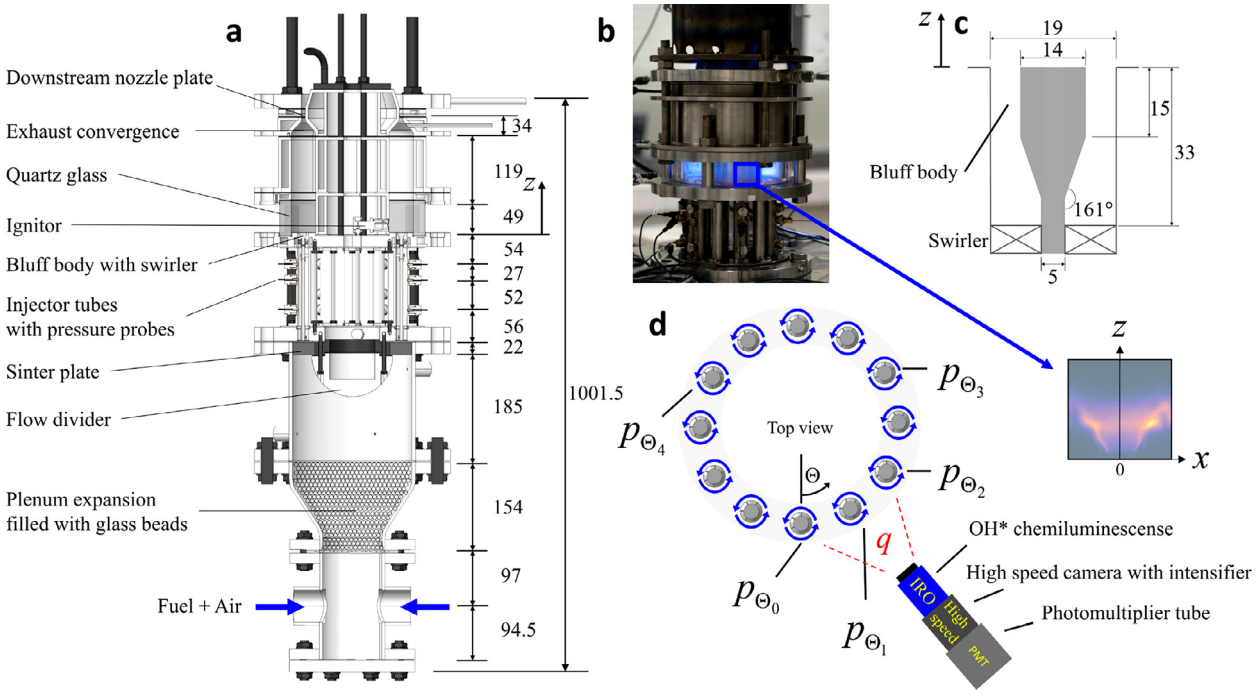

Fig. 1. (a) Cross-section view of the Intermediate Pressure Annular (IPA) combustor, (b) Photograph of flames during self-excited azimuthal instabilities, (c) Lateral view of bluff body and swirler, (d) Top view showing azimuthal position of microphones which are located at $\Theta_{\{k=0,1,2,3,4\}} = 0, 30, 60, 120,$ and 240°. A high-speed camera and photomultiplier tube at 30° capture the HRR response. All dimensions in mm.

The combustion chamber has a length $l_c = 168$ mm, with inner and outer walls of diameter $d_i = 128$ mm and $d_o = 212$ mm respectively. The combustor outlet is defined by a two-stage annular nozzle. Across the first stage, a contraction ratio of $CR = 7$ occurs over a length $l_{CR} = 34$ mm. The second contraction occurs as the flow passes a replaceable blockage plate, providing a total area contraction ratio of $CR_{\text{total}} = 33$. The blockage plate results in a continuous annular exit gap of width 1.18 mm at a mean diameter of 164.75 mm. The lower section of the outer annular wall is made out of a quartz glass, in order to provide optical access. The remaining outer and inner walls and the dump plane are stainless steel and are water-cooled, utilizing three separate cooling circuits. The cooling heat transfer is estimated based on water inlet/outlet temperatures and flow rates for these three circuits as $P_{\text{cool}-\text{i}} \approx 100$ kW, $P_{\text{cool}-\text{o}} \approx 50$ kW, and $P_{\text{cool}-\text{d}} \approx 15$ kW.

The mass flow rates of air and fuel were controlled using four Alicat Mass flow controllers (MFC), two for air, and one each for CH_4 and H_2. The range of the air and fuel MFCs are 5000 SLPM and 1000 SLPM respectively. Each MFC has an accuracy of ±0.8% of the reading plus ±0.2% of the full scale. The reactants are supplied at a mean temperature of approximately 293 K. The equivalence ratio was varied between 0.7 to 1.0, while the air mass flow rate was maintained constant at 95.7 gs^{-1}. The volume fraction of hydrogen, $P_V = \dot{V}_{H2}/(\dot{V}_{CH4} + \dot{V}_{H2})$, was varied from 0.25 to 0.43. This range corresponds to thermal power ratio of hydrogen, P_H, from 0.10 to 0.20. The bulk flow velocity, u_b, is evaluated at the dump plane based on the volumetric flow rates. Finally, a total of three repeat runs were performed for each operating condition.

2.2. Instrumentation and data acquisition

Pressure sensors (Kulite XCE-093 sensors, 1.4286×10^{-4} mV/Pa) were used to measure pressure oscillations and installed at five locations around the annulus $\Theta_{\{k=0-4\}} = 0, 30, 60, 120,$ and 240° at an axial position $z = -81$ mm from the dump plane ($z = 0$ mm) as shown in fig. 1d. Three additional microphones were installed at $z = -133$ mm in the injector pipes at 0, 30, and 60°. Pressure signals were conditioned by an amplifier (Fylde FE-579-TA), and stored at a sampling rate of 51.2 kHz for a period of 60 s for each experiment. Signals were digitized by a 24-bit DAQ system (NI model 9174).

High-speed imaging was performed using a Phantom V2012 camera with a LaVision Image Intensified Relay Optics (IRO) unit, fitted with a 100 mm Cerco 2178 UV lens. The high-speed camera was positioned at $\Theta_{\{k=1\}} = 30^\circ$ at a horizontal distance from the quartz glass of 0.6 m. A photomultiplier tube (PMT) is positioned in parallel to capture the same region of interest, corresponding to a single flame, as shown in fig. 1d. A narrow bandpass filter (centered at 310 nm, with a full width at half maximum of 10 nm) is mounted to both the camera and PMT in order to capture the OH* response, which is used as a proxy for the HRR [49]. A total of 80,000 images were sampled for each case at a rate of 16 kHz, with a region of interest of 535 × 560 pixels, giving a spatial resolution of 0.09 mm/pixel.

2.3. Pressure propagation and mode characterization

The pressure response is characterized by azimuthal modes of varying order, n. The current paper focuses only on modes of order $n = 1, 2$, which are referred to as the fundamental and first harmonic modes. The mode of oscillation is determined at each frequency of interest using the approach outlined by Ghirardo *et al.* [50], where the acoustic pressure oscillations in the system, p', are described according to

$$p'(\Theta, t) = A\cos(n(\Theta - \theta))\cos(\chi)\cos(\omega t + \varphi) + A\sin(n(\Theta - \theta))\sin(\chi)\sin(\omega t + \varphi), \quad (1)$$

where Θ is the azimuthal coordinate, A is the amplitude of the mode, θ is the position of the anti-nodal line and φ describes the slowly varying phase. The variable χ describes the nature of the mode, and indicates whether the azimuthal eigenmode is a standing wave, $\chi = 0$, a pure clockwise or counter-clockwise spinning

wave, $\chi = \mp\pi/4$, or a mix of both for $0 < |\chi| < \pi/4$. The spin direction is based on viewing the combustor dump plane from overhead (a location downstream) as shown in the coordinate system in fig. 1.

The mode nature angle is evaluated upstream of the combustor at a location $z = -81$ mm, as five transducers at this axial location can be used to assess the mode using equation 1. While the calculation of the mode nature angle and orientation does not depend on the axial location at which they are evaluated, the amplitude of the mode A does vary with axial location along the duct. It is therefore of interest to describe the pressure oscillations at the dump plane to be able to investigate the HRR signal relative to the pressure signal at the exit of the injector.

To propagate the pressure and calculate velocity oscillations, we calculate the acoustic field in the injector. The swirler has a strong effect at high frequencies, which is taken into account using a scattering matrix approach. The acoustic field in the injector tube is described by

$$p'(z,t) = \Re((B^+ \exp(-ik^+ z) + B^- \exp(ik^- z)) \exp(i\omega t)), \quad (2)$$

where B^+ and B^- describe the complex amplitudes and k^+ and k^- the wave numbers of a downstream and upstream traveling wave respectively. The wave amplitudes are calculated with the multiple microphone method [51], which assumes the presence of 1D plane waves, and is valid only in the injector pipe. The method can also be used to calculate the acoustic velocity field in the injector tube.

$$u'(z,t) = 1/(\bar{\rho}\bar{c})\Re((B^+ \exp(-ik^+ z) - B^- \exp(ik^- z)) \exp(i\omega t)), \quad (3)$$

where $\bar{c}$ is the mean speed of sound and $\bar{\rho}$ is the mean density. The scattering matrix [52] is defined as

$$\begin{pmatrix} B_d^- \\ B_d^+ \end{pmatrix} = \begin{pmatrix} S_{11} & S_{12} \\ S_{21} & S_{22} \end{pmatrix} \begin{pmatrix} B_u^+ \\ B_u^- \end{pmatrix}, \quad (4)$$

where the subscript u and d denote the elements upstream and downstream of the swirler. The frequency-dependent scattering matrix of the swirler is taken from [42]. Finally, the pressure oscillations are propagated from the trailing edge of the swirler to the dump plane. This distance involves a continuous area change through the expansion of the bluff body, which is approximated by a series of discrete area changes through pressure and mass flow conservation laws. The propagation method was compared with an acoustically forced reference case under cold flow conditions where a microphone was placed at the exit, and found to be reliable up to a frequency of ~ 3.5 kHz. Therefore, only the fundamental and first harmonic modes are propagated in the current work. Mean pressure amplitude and phase errors for $n = 1$ and $n = 2$ modes of around 10% and 15%, and $\pm 10^\circ$ and $\pm 40^\circ$ were found respectively.

2.4. Heat release rate response analysis

The spatially distributed HRR, $q(x,z,t)$, is measured by the camera, which integrates OH* intensity along each pixel's line of sight. The spatial coordinates represent the intersection of the lines of sight with a calibration plane, centered on the bluff body of the injector at $\Theta = 30^\circ$. This HRR can be temporally decomposed into the time-averaged HRR, $\bar{q}(x,z)$, the phase-dependent fluctuating component, $q'(x,z,t)$, and the stochastic fluctuations, $q''(x,z,t)$:

$$q(x,z,t) = \bar{q}(x,z) + q'(x,z,t) + q''(x,z,t). \quad (5)$$

The phase-dependent fluctuating component, $q'(x,z,t)$, can be evaluated through either phase averaging or spectral approaches. In the current work, tilde notation $\tilde{(\cdot)}$ is used to explicitly refer to the former. Therefore, $\tilde{q}(x,z,t)$ is the phase-dependent fluctuating component which is evaluated by conditional averaging of the images. Phase averaging is performed with respect to the phase angle of the integrated HRR from the image into 10 bins, and subtracting $\bar{q}(x,z)$, which eliminates contributions from the stochastic component ($q''(x,z,t) \to 0$) when the number of samples is large.

The global flame response is also a quantity of interest, and can be evaluated by spatially integrating the HRR from the imaging measurements. A second independent measurement of the global flame response is obtained using the PMT. A comparison of these was conducted (not presented for brevity), with a similar amplitude and phase captured using both methods, verifying the alignment of the PMT on a single flame sector. In the present manuscript, only the PMT measurements are used to evaluate the global fluctuations, due to its improved frequency resolution, signal length, and bit depth in comparison with the camera measurements.

In the current work, hat notation $\hat{(\cdot)}$ is used to express the Fourier transform, and overline notation $\overline{(\cdot)}$ is used to express time averages. Thus, the phase-dependent HRR fluctuations evaluated using spectral methods are for example expressed as the complex-valued quantity $\hat{q}(f)$, which varies as a function of the oscillation frequency, f. The normalized amplitude of the heat release oscillations is therefore expressed as $|\hat{q}|/\bar{q}$, and the phase angle of these as $\angle\hat{q}$.

2.4.1. Spatial Fourier mode decomposition

In order to investigate the spatial HRR response, a Fast Fourier Transform was performed on the image time series, $q(x,z,t)$, for each individual pixel on the camera sensor, yielding the complex-valued field, $\hat{q}(x,z,f)$, which can be interrogated at each frequency of interest with a cut-off band frequency of ± 10 Hz. The combination of imaging frequency and number of samples results in a frequency resolution of 2 Hz. Through this approach the oscillation magnitude and phase can be evaluated spatially for each of the modes fundamental and harmonic components, allowing the structure of these components to be understood. This is performed by reconstructing the oscillations for each Fourier mode through the cycle as $q'_{\mathrm{rec}}(x,z,t/T) = \Re\left(\hat{q}(x,z)e^{i2\pi t/T}\right)$.

In order to study HRR timing in the streamwise direction, phase-space diagrams of the HRR oscillations can be constructed, as used previously in for example [53,54]. The HRR is first integrated in the transverse x direction, $q_x(z,t) = \int q(x,z,t)dx$, and then the Fourier transform at each vertical location z of the integrated HRR is taken for each frequency of interest, to calculate the complex quantity, $\hat{q}_x(z)$. Phase-space diagrams are then produced by reconstructing the time series of HRR $q'_{\mathrm{rec,x}}(z,t/T) = \Re\left(\hat{q}_x(z)e^{i2\pi t/T}\right)$. Due to the significant magnitude of the harmonic components in this work, a diagram can be constructed for not only the fundamental frequency, but also the higher harmonic components, again providing insight into their dynamics.

2.4.2. Rayleigh criterion and Rayleigh index analysis

The phase lag between the propagated pressure at the dump plane and the HRR oscillations describe a necessary condition for instability through the Rayleigh criterion [55]. This phase lag can be described by the phase difference $\Delta\psi_{p-q} = \angle\hat{p} - \angle\hat{q}$.

To identify spatial regions which induce either driving or damping, two-dimensional Rayleigh index maps were computed, integrated over a measurement duration of $\tau = 0.5$ s. The Rayleigh index, RI, is defined as the time integral of the oscillating HRR and pressure in Eq. 6,

$$RI(x,z) = \tau^{-1} \int_\tau p'(z=0,t)q'(x,z,t)dt \quad (6)$$

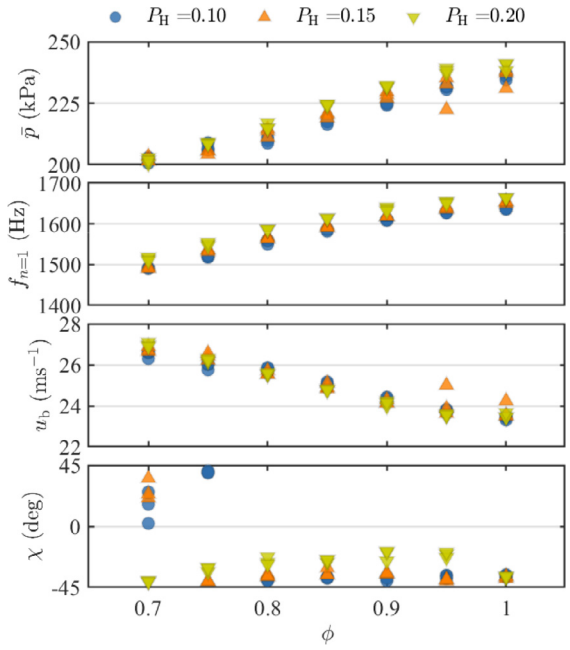

Fig. 2. Effect of equivalence ratio and power fraction of hydrogen on mean chamber pressure, fundamental frequency, bulk velocity, and nature angle. Symbol indicates $P_H = 0.10$, 0.15, and 0.20. The nature angle at the fundamental frequency is calculated by the Quaternion formalism with five pressure sensors azimuthally positioned at $\Theta_0 - \Theta_4$ as shown in fig. 1. The mean chamber pressure is evaluated at a location $z = -81$ mm, as an average of the 5 azimuthally spaced pressure sensors.

where t is time, $p'(z = 0, t)$ is the pressure oscillation at the dump plane, and $q'(x, z, t)$ is the spatial distribution of phase-dependent HRR oscillations.

3. Pressure and heat release rate oscillations

While a detailed analysis can be found in Indlekofer *et al.* [42], the combustor response to changes in operating condition is summarized here. Figure 2 shows the influence of P_H and ϕ on the time-averaged chamber pressure $\bar{p}$, bulk velocity u_b, nature angle χ, and fundamental mode frequency $f_{n=1}$. The mean chamber pressure, $\bar{p}$, is evaluated at $z = -81$ mm, as an average of the 5 azimuthally spaced pressure sensors. As ϕ increases, $\bar{p}$ and $f_{n=1}$ increase gradually. In contrast, u_b decreases with increasing ϕ due to the increase of gas temperature and mean chamber pressure. The downstream outlet nozzle is always choked, as $\bar{p} \geq 200$ kPa. There is a weak dependence on P_H at a given ϕ. Increasing P_H increases the adiabatic flame temperature, slightly increasing both frequency and mean pressure. While not shown here for brevity, the power increases with equivalence ratio but not significantly with hydrogen power fraction [42].

The nature angle evolves from positive to negative as equivalence ratio and hydrogen content increase. Most points are close to -45°, meaning the system predominantly couples to strongly spinning clockwise modes. For the $P_H = 0.20$ case, mixed modal behavior occurs when the pressure oscillation amplitude is relatively low at $\phi = 0.8$ to 0.9. As discussed in [42], the nature angle dependence is a result of the relative increase in noise for low amplitude cases, resulting in an increasing preference for standing modes [16,35,37].

Figure 3 shows the effect of P_H and ϕ on the behavior of the normalized pressure and HRR oscillation amplitudes, at an azimuthal location of $\Theta = 30°$. Symbol colors denote the mode order, and repeat runs are included to illustrate repeatability.

Figure 3 a shows the propagated pressure response at the dump plane, $z = 0$ mm for $n = 1, 2$ modes. For the $P_H = 0.10$ case an initially stable state occurs at $\phi = 0.7$ with very low amplitude oscillations. As ϕ increases, the system transitions to a high-amplitude instability, with the amplitude of the pressure oscillations at the fundamental frequency varying from 1.2 to 1.5% of the mean pressure. The response is also characterized by harmonics with significant amplitude as reported previously [42]. As P_H increases, the stability boundary of the system moves to lower equivalence ratios, and the pressure oscillation amplitude decreases. The propagated pressure oscillation amplitudes have a similar distribution to previously reported upstream measurements [42], but the amplitudes are significantly larger in the combustion chamber. After propagation, the amplitude at the dump plane varies from around 1.6 to 2.6 times that at $z = -81$ mm, depending on the operating conditions.

The HRR at $\Theta = 30°$ for the $n = 1$ mode in fig. 3b shows a very similar distribution to the propagated pressure response. The amplitude of the fundamental mode is significant, peaking at approximately 9% of the mean HRR. However, the first harmonic amplitude is small for all conditions, reaching a maximum of around 0.3% of the mean HRR. Therefore, despite the amplitude of the fundamental and harmonic pressure components being of the same order of magnitude during high amplitude instability, the HRR oscillations of the first harmonic are over an order of magnitude lower than the fundamental. This indicates that only the fundamental heat release response is dynamically important. This will be investigated further in §4.2.

To further quantify the HRR response to self-excited oscillations, fig. 4 shows the dependence of these on the velocity fluctuation amplitudes at the dump plane for the fundamental mode and first harmonic. The velocity is chosen here (as opposed to the pressure) as a more common way to present the flame response. Points are colored by the mode nature angle, which illustrates that high amplitude instabilities are coupled to strongly spinning modes.

To create a conventional Flame Describing Function (FDF), the flame should be subject to forced oscillations over a range of frequencies and amplitudes, at a single operating condition. Several previous studies in annular geometry have observed an approximately linear flame response (equivalent to an almost constant FDF gain), while exploring a range of amplitude responses through either acoustic forcing [56], or the time varying behaviour during intermittent self-excited bursts [57]. The linear response in the latter study is more difficult to interpret due to the very high amplitude of acoustic oscillations, which may give rise to non-linear behaviour. However, in both these studies the response is evaluated at a single operating condition. Figure 4 instead shows a scatter plot of the self-excited limit cycle response over the same range of ϕ and P_H conditions presented in fig. 3. Therefore, this plot does not show the response of the linearly stable flames as in [56], but instead shows the limit cycle behaviour at different operating conditions, where the amplitude is controlled by nonlinearities. Varying the operating condition has a small effect (maximum of 10 to 15% change) on f, u_b and $\bar{p}$ (shown previously in fig. 2), but a more significant effect on the laminar flame speed, S_L, which changes by a maximum of 44% between the different operating conditions. The laminar flame speed, S_L is computed with Cantera [58] using the GRI 3.0 mechanism for combustion kinetics. However, despite these changes in operating conditions, the limit cycle responses show an approximately linear dependence for both $n = 1, 2$ components.

One possible interpretation for the linear behavior is the acoustic losses in the system. The instability amplitude grows until the acoustic source strength is balanced by acoustic losses. Changing operating conditions may change the gain and phase of the HRR response. However, if the amount of damping does not vary signif-

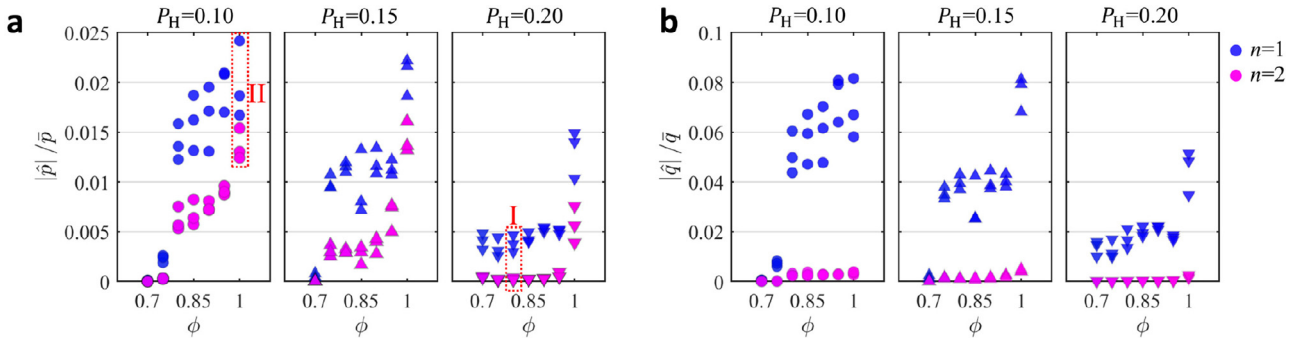

Fig. 3. Normalized (a) propagated pressure oscillation amplitude at $z = 0$ mm for $n = 1, 2$ components and (b) HRR oscillation amplitude. Each quantity is plotted against equivalence ratio at a single azimuthal location of $\Theta = 30^\circ$. HRR oscillations are based on PMT measurements. From left to right, $P_H = 0.10$ (circle), 0.15 (up-pointing triangle), and 0.20 (down-pointing triangle). Mode components are illustrated as blue ($n = 1$), magenta ($n = 2$).

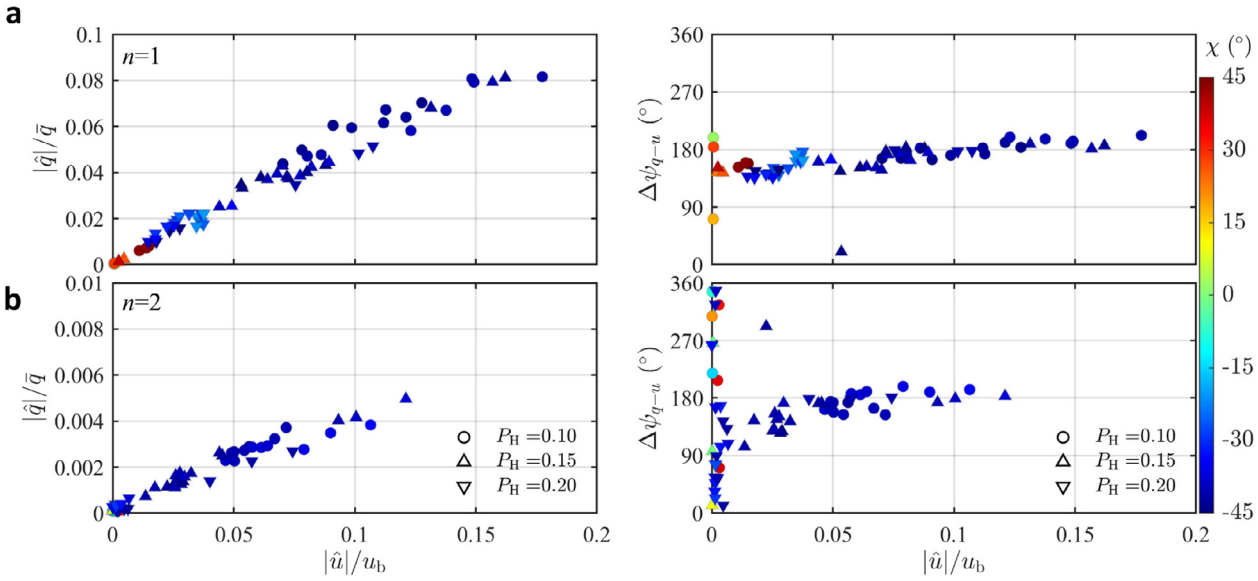

Fig. 4. Scatter plots of velocity and HRR fluctuation magnitude and phase for (a) fundamental and (b) first harmonic modes. Each data point represents the limit cycle behaviour for a different operating condition. The propagated velocity perturbation at the dump plane ($z = 0$ mm) was used, and the HRR response is from PMT measurements. Symbols indicate $P_H = 0.10$ (circle), 0.15 (up-pointing triangle), and 0.20 (down-pointing triangle). The color of the data points indicates the nature angle.

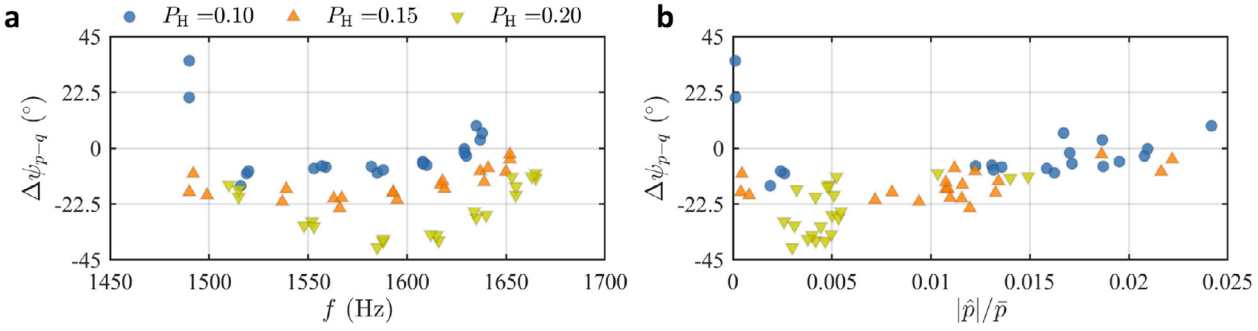

Fig. 5. Rayleigh criterion plotted against (a) fundamental mode frequency and (b) normalized pressure amplitude for the fundamental mode. Phase relation is calculated with propagated pressure signal at the dump plane ($z = 0$ mm, $\Theta = 30^\circ$), with heat release response from PMT measurements. Color-coded symbols indicate $P_H = 0.10$ (circle), 0.15 (up-pointing triangle), and 0.20 (down-pointing triangle). Data points correspond to the fundamental mode in the fig. 3b.

icantly with operating conditions and scales linearly with $|\hat{u}|/u_b$, the limit cycle amplitudes may scale linearly. This would imply that the linear slope for both $n = 1, 2$ modes is related to the amount of damping in the system.

The phase relation between the velocity and limit cycle HRR oscillations, $\Delta\psi_{q-u}$, show a slow increase in phase with oscillation amplitude. The phase of the first harmonic shows a similar trend, albeit with more scatter compared to the fundamental component.

In fig. 5 the delay between heat release rate and pressure oscillations, $\Delta\psi_{p-q}$, is plotted against the frequency and the propagated pressure oscillation amplitude. These are again plotted for the same range of ϕ and P_H conditions presented in fig. 3. As hydrogen power fraction P_H increases, the magnitude of the phase difference, $|\Delta\psi_{p-q}|$ increases for a given frequency (shown in fig. 5a) and the amplitude generally decreases (shown in fig. 5b), which is in agreement with the Rayleigh criterion. The phase dif-

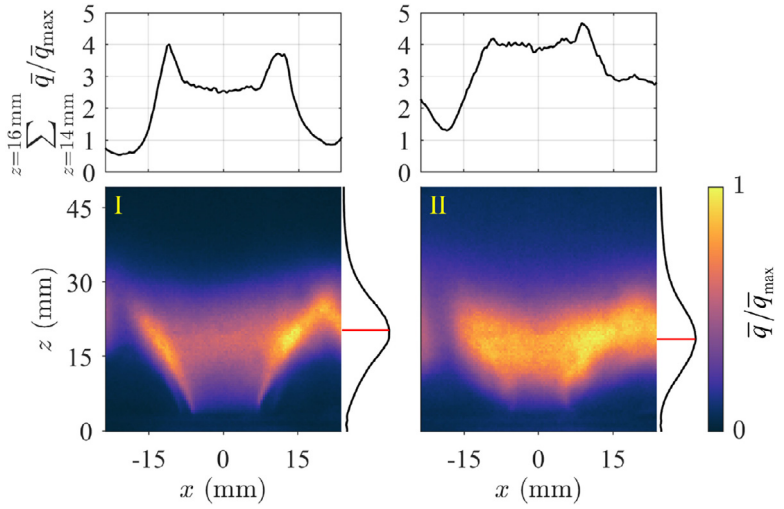

Fig. 6. Spatial distribution of normalized time-averaged HRR as a function of P_H and ϕ for cases I and II. The HRR distribution integrated in the z direction (from z=14 to 16 mm) is shown above each image to quantify the asymmetry. The HRR distribution integrated in the x direction across the entire flame is shown on the right hand side of each image. The red line indicates the flame height estimate, H_f.

Table 1
Operating conditions and variables for two cases of interest.

Case	P_H	ϕ	S_L (ms^{-1})	f (Hz)	$\lvert\hat{p}\rvert/\bar{p}$	χ (°)	u_b (ms^{-1})
I	0.20	0.8	0.30	1587	0.004	-28.1	25.6
II	0.10	1.0	0.36	1637	0.019	-36.4	23.3

ference varies with the hydrogen power fraction, which is consistent with the findings of Chterev and Boxx [11].

4. High-speed flame imaging analysis

4.1. Effect of P_H and ϕ on flame dynamics

Following a description of the global pressure and HRR responses, the effect of the former on the mean flame geometry and dynamics is investigated for two cases of interest (I and II marked in fig. 3). These two cases are selected in order to examine low and high amplitude instabilities. In table 1, the operating conditions and some important parameters are listed for the two selected cases.

First, the mean flame shape is presented in fig. 6, which shows the time average HRR normalized by the maximum OH* intensity, $\bar{q}/\bar{q}_{\max}$. The turbulent flame brush is anchored on the inner shear layer, with the maximum HRR location occurring around 20-25 mm downstream of the dump plane. Flame height decreases slightly with increasing forcing amplitude, rather than responding to changes in the bulk flow velocity or flame speed through ϕ or P_H. Therefore, slightly longer and shorter flames are observed in cases I and II, which experience low and high amplitude oscillations respectively.

The flame height variation, which is defined as the distance from the dump plane to the maximum time-averaged HRR location is presented for a range of cases in fig. 7. As expected based on the almost constant phase delay shown previously in fig. 4 and the similar bulk flow velocities, the flame length is relatively constant for high amplitude oscillations.

Figure 6 also shows that the flame structure is asymmetric, with higher mean HRRs on the right hand side. The level of asymmetry appears to grow with increasing instability amplitude, and the spatial distribution of HRR changes. For approximately axisymmetric flames, the integrated line of sight images recorded by the camera usually show the highest intensities at the sides of the

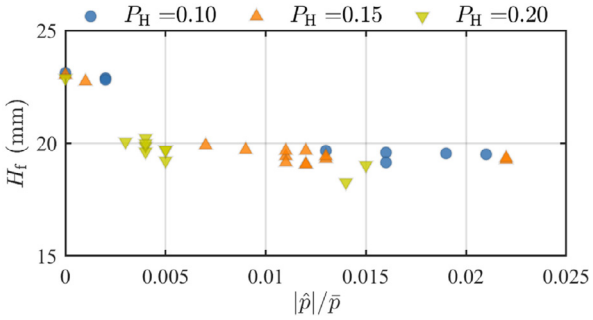

Fig. 7. Variation of flame height with normalized pressure amplitude. Flame height is defined as the vertical distance from the dump plane to the maximum HRR location of the time-averaged HRR, integrated in the transverse direction.

flame, as in case I, which is simply because more OH* intensity is integrated along the camera's lines of sight in these peripheral regions. However, as the oscillation amplitude increases the spatial distribution of intensity changes, and in case II the intensity in the centre of the flame is approximately the same as that at the left hand side. This is quantified through the line plot shown above each subplot, in which the HRR has been integrated in the z direction from $z = 14$ to 16 mm. This suggests a departure in the unsteady structure of the flames away from axisymmetry.

To understand the flame dynamics, the normalized phase-averaged HRR distributions, $\tilde{q}/\tilde{q}_{\max}$, are presented in fig. 8 at five points in the cycle. Each sequence is normalized by the maximum intensity in the cycle.

During the instability, HRR oscillations are formed and advected downstream. The response on the left and right hand side of the flame differ slightly in both phase and amplitude, with the asymmetric flame shape leading to more HRR on the right hand side and more flame-flame interaction.

Similar asymmetry has been observed previously [23,56], and results from the combination of azimuthal and axial velocity oscillations. Azimuthal velocity fluctuations result in a flapping motion [23], which occurs twice per oscillation cycle. Axial velocity oscillations result in a pulsing of the inlet flow once per oscillation cycle (c.f. [59]). As both motions affect shear layer roll-up (c.f. [60] for transverse oscillations and [61] for axial oscillations) the combination of these therefore results in asymmetry, as the axial

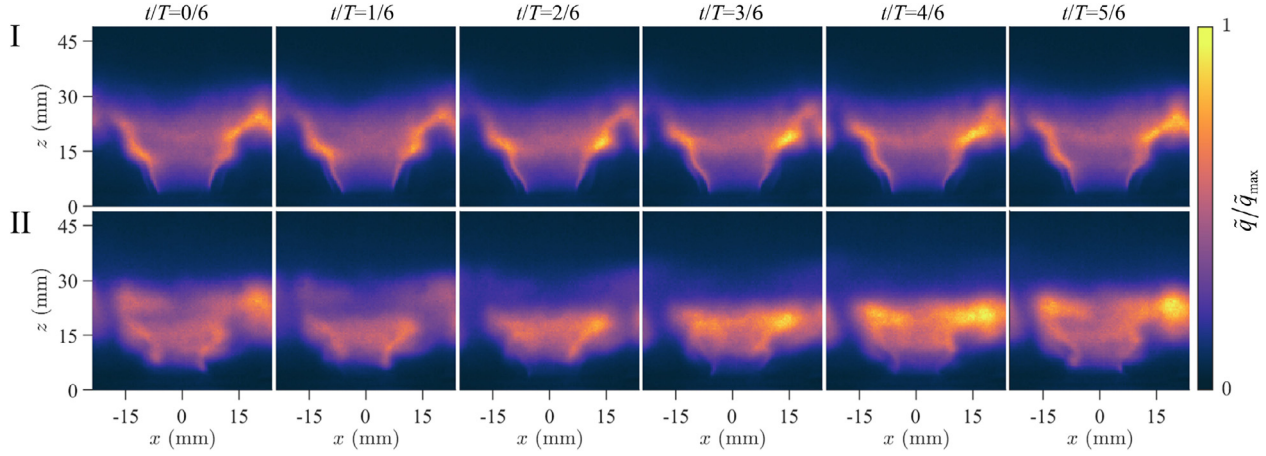

Fig. 8. Phase averaged normalized HRR dynamics for cases I and II. Spatial HRR is normalized by the maximum phase averaged intensity.

pulsing motion is associated with a flapping motion in only one azimuthal direction.

The modest oscillation level for case I results in only slight flame height variations, and no significant side-to-side motion. In comparison, a distinct side-to-side flapping is observed in case II, which is characteristic of azimuthal excitation [23]. This motion is clearly visible close to the flame base, where the flame brush efflux angle tilts from left at $t/T = 0/6$ to right at $t/T = 3/6$. At the flame tip, the structure fragments and pinches-off at around $t/T = 0/6$ to $t/T = 1/6$, resulting in sudden absence of OH* in the upper half of the images by $t/T = 2/6$. This significant flame surface annihilation results in a significant oscillation in flame height.

4.2. Fourier analysis and Rayleigh index maps

Figure 9 shows the spatial HRR oscillation amplitudes for cases I and II. These are obtained through Fourier mode reconstruction (described in §2.4.1) at four phase angles. The sum of components is presented in the top row of each subfigure, to illustrate the overall spatial response. The left hand side of each figure shows the weighted phase representation [62] of each Fourier mode, where brightness and color at each pixel location are determined by the fluctuation magnitude and phase respectively.

For case I and $n = 1$, at $t/T = 0$, oscillating bands of positive and negative amplitude can be seen along the flame brush. The oscillations are smallest at the flame base, and increase in magnitude as they are advected downstream. Structures on the left and right hand sides of the flame show subtle differences in amplitude and size, with larger magnitude oscillations shown on the right hand side. The structure on the left hand side shows both an inner and outer structure, with a slight delay in phase. The shift in phase between these two inner and outer structures reduces the magnitude of the integrated oscillation from this part of the flame.

A similar pattern occurs for the $n = 2$ mode, with a larger number of smaller structures due to the higher frequency. The first harmonic changes the maximum amplitude of the overall spatial HRR oscillations (upper row), by around 15% in comparison with the fundamental mode alone. However, the significant number of oscillations simultaneously present on the flame for the $n = 2$ mode result in the low integrated oscillation amplitudes shown previously in fig. 3b.

In comparison, the much higher magnitude oscillations in case II show a very different set of dynamics. The $n = 1$ mode oscillations are dominated by a single high amplitude band in the upper half of the flame, due to the large pinch-off event shown in fig. 8. Unlike the low amplitude oscillations, the band has high intensity both on the sides and centre of the flame; suggesting asymmetric flame dynamics. From the weighted phase plot on the left hand side, high intensity HRR oscillations only occur during a narrow range of phases in the cycle, and therefore, there is less cancellation of local HRR oscillations in this case, resulting in the high amplitude integrated response.

The asymmetry is clearly visible for the first harmonic, as the downstream location of fluctuations on left and right hand sides of the flame is staggered, due to the strong transverse flapping motion. Again, while these have some effect on the overall local oscillation amplitude, the spatially integrated influence of these is small.

The response timing or phasing can be understood by constructing phase-space plots using the method outlined in §2.4.1. The transversely integrated response is plotted as a function of downstream distance, as shown in fig. 10. Phase-space distributions are shown for case I and II, for modes of order $n = 1, 2$. Distributions are also divided by spatial extent, considering the entire flame (denoted A), with separate plots for left and right hand sides (denoted L and R respectively).

The $n = 1$ mode for the entire flame in case I is shown in fig. 10a1A. The angled streaks show HRR oscillations which are advected downstream. It is interesting to separate left and right hand sides, which for the fundamental mode are shown in fig. 10a1L and a1R. The larger magnitude oscillations on the right hand side are clearly visible in this representation, but so too is a small phase difference in the response, which can be seen comparing locations of horizontal lines representing the local cycle maximum. Similar streak structures on the right hand side have a small lag in phase in comparison with the left hand side, which has a minor cancellation effect when integrated. Large differences in phase and amplitude are also observed in the harmonic contributions.

The phase-space distributions for case II show a number of differences. The fundamental mode for the entire flame is shown in fig. 10b1A, which shows fewer but larger streaked regions in comparison with case I. The streak width is significantly increased despite similar frequencies and bulk flow velocities. The injector contains swirl vanes that act as a source of convective velocity oscillations [53,63]. In the absence of interference effects between acoustic and convective sources of velocity oscillation, the streak width should be a result of the estimated convective wavelength, which scales with frequency and bulk flow velocity, $\lambda \approx u_b/f$. However, in the presence of the swirler, modest changes in f and u_b can alter the interference between these sources, modifying the

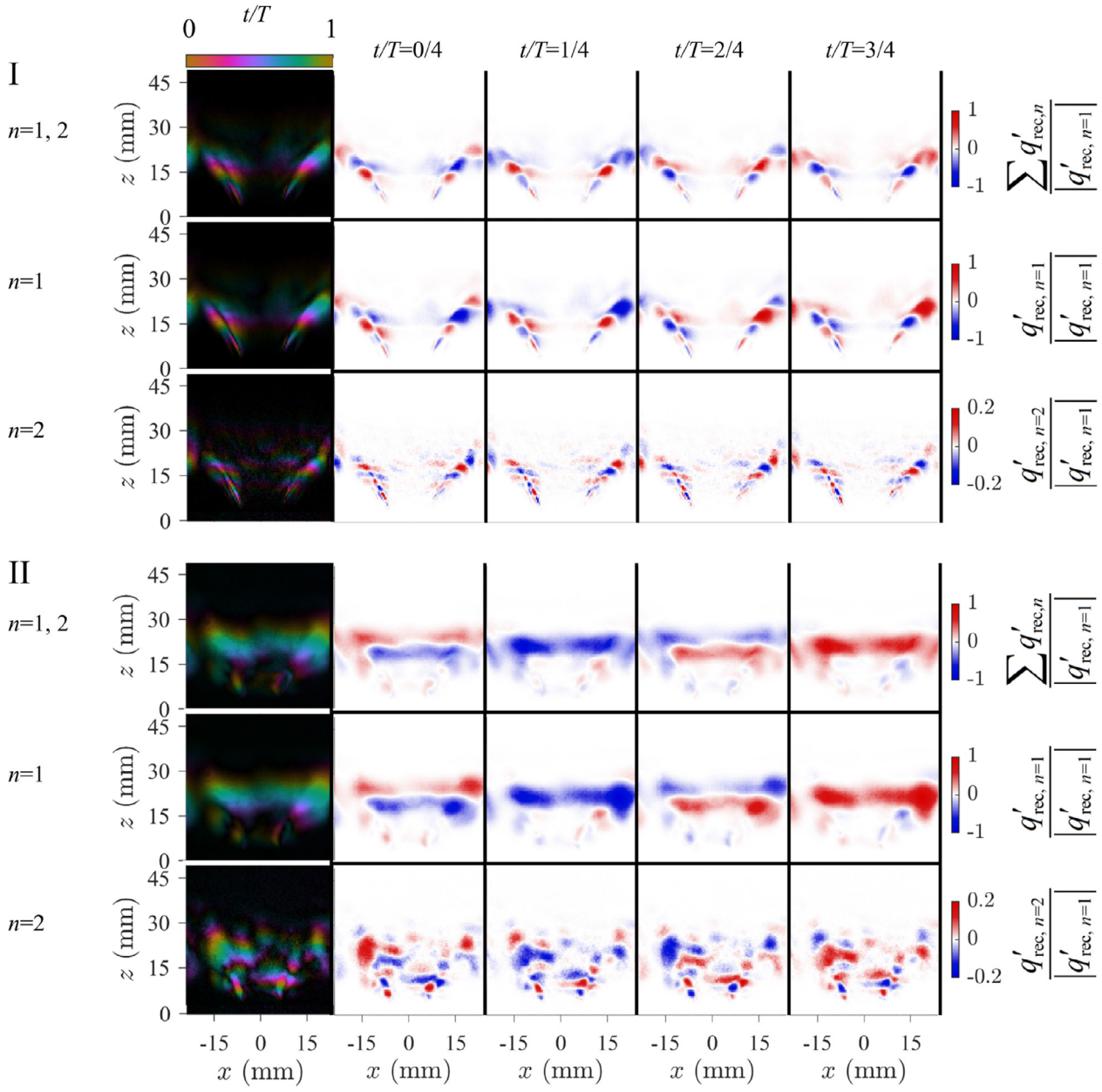

Fig. 9. Fourier mode amplitude distributions for cases I and II, presented as weighted phase plots (*left*) and a sequence of the time evolution of the normalized spatial heat release fluctuation intensity based on fundamental and harmonic Fourier modes (*right*). From top to bottom in each sub figure show the integration of first two modes, and isolated modes $n = 1, 2$.

streak width [63]. The large changes in streak width shown here are more consistent with the different interference regimes presented in [63], than expected changes due to minor differences in f and u_b. The streak width is quantified for the fundamental mode (cases a1A and b1A) at the t/T corresponding to the maximum HRR in the cycle. The width is evaluated as the distance along this line where the oscillation amplitude is greater than 50% of the maximum value. These width calculations are shown schematically with green arrows in fig. 10. The change in estimated convective wavelength between cases I and II is only approximately 6%, and should result in a shorter wavelength for case II. However, the width of the streak lines change by approximately 27.4%, and show a longer convective wavelength for case II. The increased width of the streaks results in less cancellation of the HRR when integrated spatially, consistent with the higher amplitude oscillations and the large scale pinch-off dynamics at the flame tip.

For case II, slight differences in phase occur between left and right hand sides. While the response amplitude for $n = 1$ is larger on the right hand side, the amplitude for $n = 2$ is larger on the left hand side, and for this harmonic a very different phase-space distribution is observed in the lower portion of the flame. While the right hand side of the $n = 2$ distribution resembles that of case I, the left hand side shows two distinct regions at different downstream distances, with a phase jump between them. This may imply the presence of several distinct vortical structures on the left hand side of the flame.

To identify regions of driving and damping, the Rayleigh index is plotted in fig. 11 for the two cases of interest. Pressure and HRR time series were bandpass-filtered with a bandwidth of 5 Hz.

HRR oscillations, which are both in and out of phase with the pressure oscillations, are observed as alternating regions of driving and damping respectively. These regions are largely aligned in

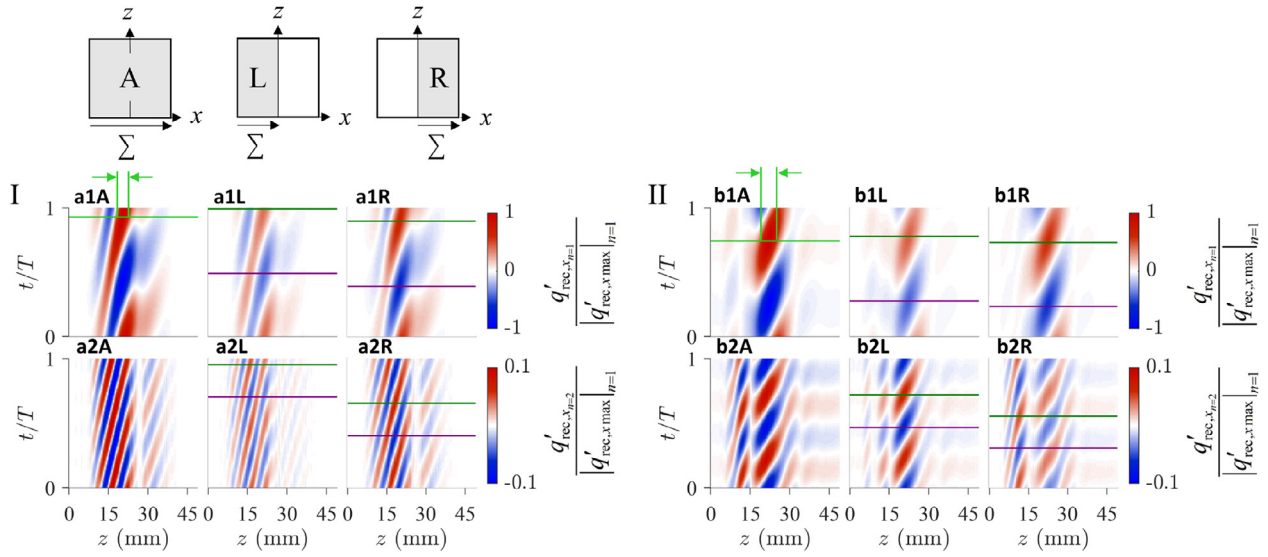

Fig. 10. Phase-space distribution of HRR oscillations for cases I and II. HRR intensity fluctuations are integrated in the transverse direction over the full field of view (A), left hand side (L), and right hand side (R). The reconstructed distributions are presented for the Fourier mode of fundamental (1), first (2) harmonic modes. These are integrated in the transverse direction over the full field of view. In these representations the streamwise flow direction is left to right. Green and purple horizontal lines indicate maximum and minimum intensity during one cycle, respectively.

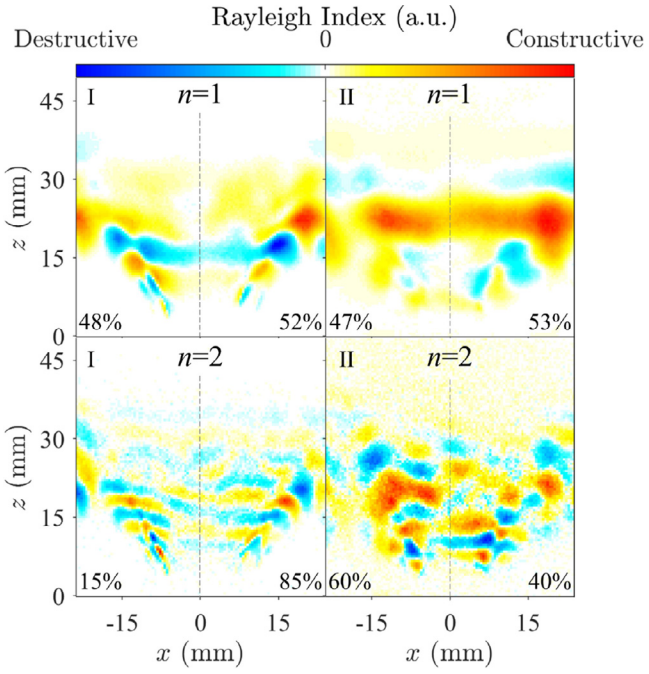

Fig. 11. Spatial distribution of Rayleigh Index for the two cases of interest. Spatially integrated percentage of driving on the LHS and RHS is indicated for each case.

the horizontal direction, and the maximum region of driving occurs at the flame tip. While case I features modest damping, case II is dominated by driving at the flame tip, resulting in the larger oscillation amplitude. Asymmetry is evaluated by spatially integrating the *RI* on the left and right hand sides, and expressing this as a percentage of the total *RI*. These values are indicated on fig. 11. While the $n = 1$ distributions are slightly asymmetric as a result of the azimuthal excitation, the side with larger regions of driving also features larger regions of damping. Therefore, despite the asymmetry of the response, both sides contribute approximately equally to the total driving for the fundamental mode.

In contrast, the $n = 2$ modes feature more significant asymmetry between left and right hand sides. For cases I and II, the right and left hand side dominate respectively. However, due to their high frequency, the inclusion of harmonic components does not significantly change the integrated Rayleigh index. A change of 0.1% and 4.6% for the integrated RI for cases I and II is calculated respectively with the inclusion of the first harmonic, demonstrating that even for large amplitude oscillations these are not dynamically significant.

5. Conclusions

In the present paper, the influence of hydrogen content and equivalence ratio on the HRR response and dynamics of hydrogen/methane blended flames in a lab-scale pressurized annular combustor have been investigated.

An almost linear scaling occurs between limit cycle HRR and pressure (and velocity) oscillation amplitudes for both the fundamental and first harmonic components, despite the wide range of operating conditions. The phase of the pressure and HRR oscillations varies with hydrogen content. Increasing hydrogen content is correlated with larger phase differences and lower instability amplitudes.

High-speed imaging was used to examine cases with low and high amplitude instabilities. During high amplitude oscillations, large changes in flame height were observed, which dominated the heat release response. Oscillations on the left and right hand sides of the flame were observed to have small differences in the timing, but large differences in amplitude. Therefore, the effect of transverse oscillations primarily resulted in heat release response asymmetry, rather than significant changes to the phasing between the two sides of the flame.

Integrating these spatial responses and evaluating them as part of the Rayleigh index showed that the high amplitude case is driven by the oscillation of HRR at the top of the flame. For the lower amplitude cases more damping is observed along the flame brush, where positive HRR oscillations occur out of phase with the pressure oscillations, resulting in an overall lower amplitude response.

Declaration of Competing Interest

The authors declare that they have no known competing financial interests or personal relationships that could have appeared to influence the work reported in this paper.

Acknowledgements

This project has received funding from the European Union's Horizon 2020 research and innovation program under Grant Agreement No 677931 (TAIAC) and 765998 (ANNULIGhT).

References

[1] M.R. Bothien, A. Ciani, J.P. Wood, G. Fruechtel, Toward decarbonized power generation with gas turbines by using sequential combustion for burning hydrogen, Journal of Engineering for Gas Turbines and Power 141 (12) (2019) 1–10.
[2] M. Ilbas, A.P. Crayford, I. Yilmaz, P.J. Bowen, N. Syred, Laminar-burning velocities of hydrogen-air and hydrogen-methane-air mixtures: An experimental study, International Journal of Hydrogen Energy 31 (12) (2006) 1768–1779, doi:10.1016/j.ijhydene.2005.12.007.
[3] T. Lieuwen, V. McDonell, E. Petersen, D. Santavicca, Fuel flexibility influences on premixed combustor blowout, flashback, autoignition, and stability, Journal of Engineering for Gas Turbines and Power 130 (1) (2008) 1–10, doi:10.1115/1.2771243.
[4] D. Beerer, V. McDonell, P. Therkelsen, R.K. Cheng, Flashback and turbulent flame speed measurements in hydrogen/methane flames stabilized by a low-swirl injector at elevated pressures and temperatures, Journal of Engineering for Gas Turbines and Power 136 (3) (2014) 1–9, doi:10.1115/1.4025636.
[5] T. Boushaki, Y. Dhué, L. Selle, B. Ferret, T. Poinsot, Effects of hydrogen and steam addition on laminar burning velocity of methane-air premixed flame: Experimental and numerical analysis, International Journal of Hydrogen Energy 37 (11) (2012) 9412–9422, doi:10.1016/j.ijhydene.2012.03.037.
[6] R.K. Cheng, D. Littlejohn, P.A. Strakey, T. Sidwell, Laboratory investigations of a low-swirl injector with H2 and CH4 at gas turbine conditions, Proceedings of the Combustion Institute 32 II (2) (2009) 3001–3009, doi:10.1016/j.proci.2008.06.141.
[7] D. Kim, S.W. Park, Effects of hydrogen addition on flame structure and forced flame response to velocity modulation in a turbulent lean premixed combustor, Fuel 89 (11) (2010) 3475–3481, doi:10.1016/j.fuel.2010.06.021.
[8] D.W. Davis, P.L. Therkelsen, D. Littlejohn, R.K. Cheng, Effects of hydrogen on the thermo-acoustics coupling mechanisms of low-swirl injector flames in a model gas turbine combustor, Proceedings of the Combustion Institute 34 (2) (2013) 3135–3143, doi:10.1016/j.proci.2012.05.050.
[9] E. Karlis, Y. Liu, Y. Hardalupas, A.M. Taylor, H2 enrichment of CH4 blends in lean premixed gas turbine combustion: An experimental study on effects on flame shape and thermoacoustic oscillation dynamics, Fuel 254 (May) (2019) 115524, doi:10.1016/j.fuel.2019.05.107.
[10] J. Beita, M. Talibi, S. Sadasivuni, R. Balachandran, Thermoacoustic Instability Considerations for High Hydrogen Combustion in Lean Premixed Gas Turbine Combustors: A Review, Hydrogen 2 (1) (2021) 33–57, doi:10.3390/hydrogen2010003.
[11] I. Chterev, I. Boxx, Effect of hydrogen enrichment on the dynamics of a lean technically premixed elevated pressure flame, Combustion and Flame 225 (2021) 149–159.
[12] S. Hong, S.J. Shanbhogue, R.L. Speth, A.F. Ghoniem, On the phase between pressure and heat release fluctuations for propane/hydrogen flames and its role in mode transitions, Combustion and Flame 160 (12) (2013) 2827–2842, doi:10.1016/j.combustflame.2013.07.001.
[13] M. Wang, Y. Zhong, K. Deng, Experiment investigation of the effects of hydrogen content on the combustion instability of methane/hydrogen lean premixed swirl flames under different acoustic frequency ranges, AIP Advances 9 (4) (2019), doi:10.1063/1.5091617.
[14] T. Lee, K.T. Kim, Combustion dynamics of lean fully-premixed hydrogen-air flames in a mesoscale multinozzle array, Combustion and Flame 218 (2020) 234–246, doi:10.1016/j.combustflame.2020.04.024.
[15] E. Æsøy, J.G. Aguilar, S. Wiseman, M.R. Bothien, N.A. Worth, J.R. Dawson, Scaling and prediction of transfer functions in lean premixed H2/CH4-flames, Combustion and Flame 215 (2020) 269–282, doi:10.1016/j.combustflame.2020.01.045.
[16] N. Noiray, B. Schuermans, On the dynamic nature of azimuthal thermoacoustic modes in annular gas turbine combustion chambers, Proceedings of the Royal Society A: Mathematical, Physical and Engineering Sciences 469 (2151) (2013) 20120535, doi:10.1098/rspa.2012.0535.
[17] J.R. Seume, N. Vorbneyer, W. Krause, J. Hermann, C.C. Hantsehk, P. Zangl, S. Gleis, D. Vorbneyer, A. Orthmann, Application of active combustion instability control to a heavy duty gas turbine, Proceedings of the ASME Turbo Expo 120 (97) (1997), doi:10.1115/97-AA-119.
[18] W. Krebs, P. Flohr, B. Prade, S. Hoffmann, Thermoacoustic stability chart for high-intensity gas turbine combustion systems, Combustion Science and Technology 174 (7) (2002) 99–128, doi:10.1080/00102200208984089.
[19] N.A. Worth, J.R. Dawson, Self-excited circumferential instabilities in a model annular gas turbine combustor: Global flame dynamics, Proceedings of the Combustion Institute 34 (2) (2013) 3127–3134, doi:10.1016/j.proci.2012.05.061.
[20] N.A. Worth, J.R. Dawson, Modal dynamics of self-excited azimuthal instabilities in an annular combustion chamber, Combustion and Flame 160 (11) (2013) 2476–2489, doi:10.1016/j.combustflame.2013.04.031.
[21] N.A. Worth, J.R. Dawson, Cinematographic OH-PLIF measurements of two interacting turbulent premixed flames with and without acoustic forcing, Combustion and Flame 159 (3) (2012) 1109–1126, doi:10.1016/j.combustflame.2011.09.006.
[22] J.-F. Bourgouin, D. Durox, J.P. Moeck, T. Schuller, S. Candel, Self-sustained instabilities in an annular combustor coupled by azimuthal and longitudinal acoustic modes, Volume 1B: Combustion, Fuels and Emissions, American Society of Mechanical Engineers, 2013, doi:10.1115/gt2013-95010. V01BT04A007
[23] J.R. Dawson, N.A. Worth, Flame dynamics and unsteady heat release rate of self-excited azimuthal modes in an annular combustor, Combustion and Flame 161 (10) (2014) 2565–2578, doi:10.1016/j.combustflame.2014.03.021.
[24] G. Vignat, D. Durox, A. Renaud, S. Candel, High amplitude combustion instabilities in an annular combustor inducing pressure field deformation and flame blow off, Journal of Engineering for Gas Turbines and Power 142 (1) (2020) 1–11, doi:10.1115/1.4045515.
[25] P. Wolf, G. Staffelbach, L.Y. Gicquel, J.D. Müller, T. Poinsot, Acoustic and large eddy simulation studies of azimuthal modes in annular combustion chambers, Combustion and Flame 159 (11) (2012) 3398–3413, doi:10.1016/j.combustflame.2012.06.016.
[26] N. Zettervall, N. Worth, M. Mazur, J. Dawson, C. Fureby, Large eddy simulation of CH4-air and c2h4-air combustion in a model annular gas turbine combustor, Proceedings of the Combustion Institute 37 (4) (2019) 5223–5231, doi:10.1016/j.proci.2018.06.021.
[27] B. Schuermans, C.O. Paschereit, P. Monkewitz, Non-linear combustion instabilities in annular gas-turbine combustors, Collection of Technical Papers - 44th AIAA Aerospace Sciences Meeting 9 (January) (2006) 6634–6645.
[28] A.S. Morgans, S.R. Stow, Model-based control of combustion instabilities in annular combustors, Combustion and Flame 150 (4) (2007) 380–399, doi:10.1016/j.combustflame.2007.06.002.
[29] B. Schuermans, F. Guethe, D. Pennel, D. Guyot, C.O. Paschereit, Thermoacoustic modeling of a gas turbine using transfer functions measured at full engine pressure, Proceedings of the ASME Turbo Expo 2 (November) (2009) 503–514, doi:10.1115/GT2009-59605.
[30] P. Berenbrink, S. Hoffmann, Suppression of dynamic combustion instabilities by passive and active means, Proceedings of the ASME Turbo Expo 2 (2000) 1–7, doi:10.1115/2000-GT-0079.
[31] M. Bauerheim, P. Salas, F. Nicoud, T. Poinsot, Symmetry breaking of azimuthal thermo-acoustic modes in annular cavities: A theoretical study, Journal of Fluid Mechanics 760 (2014) 431–465, doi:10.1017/jfm.2014.578.
[32] G. Ghirardo, M.P. Juniper, J.P. Moeck, Stability criteria for standing and spinning waves in annular combustors, Volume 4B: Combustion, Fuels and Emissions, American Society of Mechanical Engineers, 2015, doi:10.1115/gt2015-43127. V04BT04A005
[33] J.R. Dawson, N.A. Worth, The effect of baffles on self-excited azimuthal modes in an annular combustor, Proceedings of the Combustion Institute 35 (3) (2015) 3283–3290, doi:10.1016/j.proci.2014.07.011.
[34] N. Noiray, M. Bothien, B. Schuermans, Investigation of azimuthal staging concepts in annular gas turbines, Combustion Theory and Modelling 15 (5) (2011) 585–606, doi:10.1080/13647830.2011.552636.
[35] A. Faure-Beaulieu, N. Noiray, Symmetry breaking of azimuthal waves: Slow-flow dynamics on the Bloch sphere, Physical Review Fluids 5 (2) (2020), doi:10.1103/PhysRevFluids.5.023201.
[36] J.-F. Bourgouin, D. Durox, J.P. Moeck, T. Schuller, S. Candel, Characterization and modeling of a spinning thermoacoustic instability in an annular combustor equipped with multiple matrix injectors, Journal of Engineering for Gas Turbines and Power 137 (2) (2015).
[37] G. Ghirardo, F. Gant, Background noise pushes azimuthal instabilities away from spinning states, arXiv preprint arXiv:1904.00213 (2019) 1–4.
[38] F. Marble, S. Candel, Acoustic disturbance from gas non-uniformities convected through a nozzle, Journal of Sound and Vibration 55 (2) (1977) 225–243, doi:10.1016/0022-460X(77)90596-X.
[39] D. Fanaca, P.R. Alemela, F. Ettner, C. Hirsch, T. Sattelmayer, B. Schuermans, Determination and comparison of the dynamic characteristics of a perfectly premixed flame in both single and annular combustion chambers, Volume 3: Combustion, Fuels and Emissions, Parts A and B, ASMEDC (2008), pp. 565–573, doi:10.1115/gt2008-50781.
[40] D. Fanaca, P.R. Alemela, C. Hirsch, T. Sattelmayer, Comparison of the flow field of a swirl stabilized premixed burner in an annular and a single burner combustion chamber, Journal of Engineering for Gas Turbines and Power 132 (7) (2010) 1–7, doi:10.1115/1.4000120.
[41] M. Mazur, Y.H. Kwah, T. Indlekofer, J.R. Dawson, N.A. Worth, Self-excited longitudinal and azimuthal modes in a pressurised annular combustor, Proceedings of the Combustion Institute 38 (2021) 1–8, doi:10.1016/j.proci.2020.05.033.
[42] T. Indlekofer, B. Ahn, Y.H. Kwah, S. Wiseman, M. Mazur, J.R. Dawson, N.A. Worth, The effect of hydrogen addition on the amplitude and harmonic response of azimuthal instabilities in a pressurized annular combustor, Combustion and Flame 228 (2021) 375–387.

[43] T.C. Lieuwen, V. Yang, Combustion Instabilities In Gas Turbine Engines: Operational Experience, Fundamental Mechanisms, and Modeling, American Institute of Aeronautics and Astronautics, 2006, doi:10.2514/4.866807.
[44] S.R. Stow, A.P. Dowling, A Time-Domain Network Model for Nonlinear Thermoacoustic Oscillations, Journal of Engineering for Gas Turbines and Power 131 (3) (2009) 031502, doi:10.1115/1.2981178.
[45] B. Giacomo, N. Noiray, Synchronization of Thermoacoustic Modes in Sequential Combustors, Journal of Engineering for Gas Turbines and Power 141 (3) (2019) 1–9, doi:10.1115/1.4041027.
[46] K.T. Kim, Nonlinear Interactions Between the Fundamental and Higher Harmonics of Self-Excited Combustion Instabilities, Combustion Science and Technology 189 (7) (2017) 1091–1106, doi:10.1080/00102202.2016.1275591.
[47] M.L. Passarelli, J.M. Cirtwill, T. Wabel, A.M. Steinberg, A. Wickersham, Synchronization during multi-mode thermoacoustic oscillations in a liquid-fueled gas turbine combustor at elevated pressure, Turbo Expo: Power for Land, Sea, and Air, volume 58622, American Society of Mechanical Engineers, 2019. V04BT04A046
[48] M. Haeringer, M. Merk, W. Polifke, Inclusion of higher harmonics in the flame describing function for predicting limit cycles of self-excited combustion instabilities, Proceedings of the Combustion Institute 37 (4) (2019) 5255–5262.
[49] S. Sardeshmukh, M. Bedard, W. Anderson, The use of OH^* and CH^* as heat release markers in combustion dynamics, International Journal of Spray and Combustion Dynamics 9 (4) (2017) 409–423, doi:10.1177/1756827717718483.
[50] G. Ghirardo, M.P. Juniper, Azimuthal instabilities in annular combustors: standing and spinning modes, Proceedings of the Royal Society A: Mathematical, Physical and Engineering Sciences 469 (2157) (2013) 20130232, doi:10.1098/rspa.2013.0232.
[51] A.F. Seybert, D.F. Ross, Experimental determination of acoustic properties using a two-microphone random-excitation technique, Journal of the Acoustical Society of America 61 (5) (1977) 1362–1370, doi:10.1121/1.381403.
[52] M. Åbom, Measurement of the scattering-matrix of acoustical two-ports, Mechanical Systems and Signal Processing 5 (2) (1991) 89–104, doi:10.1016/0888-3270(91)90017-Y.
[53] P. Palies, D. Durox, T. Schuller, S. Candel, The combined dynamics of swirler and turbulent premixed swirling flames, Combustion and Flame 157 (9) (2010) 1698–1717, doi:10.1016/j.combustflame.2010.02.011.
[54] H.T. Nygård, N.A. Worth, Flame transfer functions and dynamics of a closely confined premixed bluff body stabilized flame with swirl, Journal of Engineering for Gas Turbines and Power 143 (4) (2021) 1–10, doi:10.1115/1.4049513.
[55] L. Rayleigh, The explanation of certain acoustical phenomena, Nature 8 (1878) 536–542.
[56] H.T. Nygård, G. Ghirardo, N.A. Worth, Azimuthal flame response and symmetry breaking in a forced annular combustor, Combustion and Flame 233 (2021), doi:10.1016/j.combustflame.2021.111565.
[57] K. Prieur, D. Durox, T. Schuller, S. Candel, Strong azimuthal combustion instabilities in a spray annular chamber with intermittent partial blow-off, Journal of Engineering for Gas Turbines and Power 140 (3) (2018).
[58] D.G. Goodwin, H.K. Moffat, R.L. Speth, Cantera: An object-oriented software toolkit for chemical kinetics, thermodynamics, and transport processes. version 2.3.0.(2017). doi:10.5281/ZENODO.170284.
[59] R. Balachandran, B. Ayoola, C. Kaminski, A. Dowling, E. Mastorakos, Experimental investigation of the nonlinear response of turbulent premixed flames to imposed inlet velocity oscillations, Combustion and Flame 143 (1-2) (2005) 37–55, doi:10.1016/j.combustflame.2005.04.009.
[60] N.A. Worth, D. Mistry, T. Berk, J.R. Dawson, Vortex dynamics of a jet at the pressure node in a standing wave, Journal of Fluid Mechanics 882 (2020).
[61] S.C. Crow, F. Champagne, Orderly structure in jet turbulence, Journal of fluid mechanics 48 (3) (1971) 547–591.
[62] M. Hauser, M. Lorenz, T. Sattelmayer, Influence of transversal acoustic excitation of the burner approach flow on the flame structure, Journal of Engineering for Gas Turbines and Power 133 (4) (2011) 1–8, doi:10.1115/1.4002175.
[63] E. Æsøy, H.T. Nygård, N.A. Worth, J.R. Dawson, Tailoring the gain and phase of the flame transfer function through targeted convective-acoustic interference, Combustion and Flame 236 (2022) 111813, doi:10.1016/j.combustflame.2021.111813.